Macromolecules

ARTICLE

pubs.acs.org/Macromolecules

Mesoscale Morphology and Charge Transport in Colloidal Networks of Poly(3-hexylthiophene)

Gregory M. Newbloom, Felix S. Kim, Samson A. Jenekhe, and Danilo C. Pozzo*

Department of Chemical Engineering, University of Washington, Box 351750, Seattle, Washington 98195-1750, United States

Supporting Information

ABSTRACT: We identify and characterize the mesoscale morphology of poly(3-hexylthiophene) (P3HT) fibers crystallized through colloidal self-assembly in various aromatic solvents. The network structure of the P3HT is evaluated through *in situ* small-angle neutron scattering (SANS) and ultra small-angle neutron scattering (USANS) experiments and by electron microscopy. Through model fitting to the scattering data, we are able to determine that P3HT forms network structures in solution prior to deposition. We directly obtain structural parameters such as the fraction of P3HT in nanofiber form, the cross-sectional fiber shape, and the fractal dimension of the colloidal networks. The structural parameters are shown to be strongly dependent on the solvent choice. *Ex situ* microscopy experiments are also performed to provide complementary structural information such as type and frequency of fibrillar junctions and the network size. The structural parameters are also analyzed within the context of the hole mobility in organic field effect transistors (OFET).

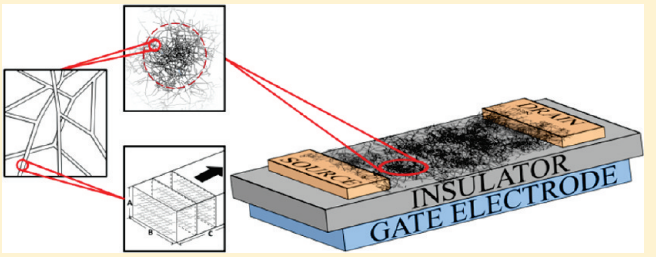

1. INTRODUCTION

Conjugated polymer semiconductors have seen a wide range of applications in the pursuit of low-cost, easy-to-manufacture electronic devices. Poly(3-hexylthiophene) (P3HT) is one of the most studied conjugated polymers due to its high hole mobility, up to 0.1 $cm^2 V^{-1} s^{-1}$, solution processability, and capacity for self-assembly.[1,2] The morphology of conjugated polymers, such as P3HT, is a critical design parameter for high-performance organic field-effect transistors (OFETs) and organic photovoltaics (OPVs).[3,4] Polymer crystallization induced by $\pi-\pi$ stacking, alkyl side-chain interactions, and solubility changes allows for an increase of conjugation length and for efficient charge transport.[5] In contrast, frequent conjugation breaks and weak π-orbital overlaps that are seen in the amorphous phase result in a decrease of charge carrier mobility.[6] An interconnected crystal network represents an ideal structure for organic semiconductor layers because it combines the high hole mobility of the crystalline domains with a continuous path for charge transport.[1,7,8]

P3HT crystallization can proceed directly in the solution phase through a preparation process that is commonly known as the "whisker method".[9,10] In this method, P3HT chains have been shown to self-assemble into orthorhombic fibers, with estimated dimensions of 2−10 nm in height, 15−25 nm in width, and many micrometers in length, in a process that is driven by changes to the solubility of the polymer.[11,12] This method has also been applied to develop high-efficiency OPVs based on poly(3-butylthiophene).[13,14] One advantage presented by generating devices using the "whisker method" is that the parameters controlling polymer self-assembly are decoupled from those that control the coating process so that both can be optimized separately. However, fabricating OPV devices from individual fiber dispersions (i.e., whiskers) may have drawbacks because the direction of the shear field applied during coating can lead to a planar orientation of the fibers with respect to the substrates and result in limited charge transport in the vertical direction.

Some researchers have also observed a branching network structure for coated crystalline P3HT dispersions using atomic force microscopy (AFM) and transmission electron microscopy (TEM).[7,15] However, limitations in resolution of such techniques prevent distinction between overlapping fibers and colloidal fiber networks. Furthermore, the analysis of coated films prevents the investigation of the structures and self-assembly directly in the dispersed state. These proposed networked structures, also obtained from self-assembly in solution, are in contrast with the individual long (>1 μm) nanofibers that are typically formed in other thin-film coating processes.[1,16] A network structure of P3HT nanofibers could be ideal for both OFET and OPV devices because the three-dimensional and interconnected fiber structure would significantly enhance charge transport in all directions. Furthermore, polymer self-assembly is decoupled from the coating process and can be optimized through controlled changes in temperature and solvent quality.

In order to optimize charge transport in these systems, it is also critical to fully understand the nature of the fiber junctions and the structure of the network. For example, fibrillar contacts and overlaps, observed in thin film crystallization, are fundamentally

Received: January 10, 2011
Revised: March 17, 2011
Published: May 02, 2011

different from fibrillar bifurcations (i.e., splitting fibers). The $\pi-\pi$ stacking structure of the thiophene ring causes insulating alkyl chains to orient in such a way that they "coat" the outside of the semiconducting fiber.[15] Charge transport between overlapping fibers requires charges to tunnel through the insulating alkyl layers. In contrast, a bifurcating fiber provides a direct, interconnected pathway for charge transport. The overall size and distribution of fibers within the network structure will also impact charge transport between electrodes. So far, these morphological features have not been explicitly considered in the design of organic electronic devices even though differences in these structural parameters could influence the electrical properties.

The present work focuses on characterizing the nature of the network structures that arise from the colloidal self-assembly of P3HT in various aromatic solvents. Understanding the mesoscopic structure of the network is critical to further optimize charge transport and to improve the performance of OFETs and OPV devices.[3] Because crystallization is a solubility-driven process, the use of different aromatic solvents allows for careful control over the intermolecular interactions between P3HT and the solvent.[12] In addition, this study evaluates the network structure directly *in situ* using small-angle neutron scattering (SANS) and ultra small-angle neutron scattering (USANS). Previous researchers have primarily utilized various *ex situ* microscopy techniques to evaluate these networks even though the coating and drying process could significantly affect the structures observed in microscopy images.[17] In this study, the fibrillar and network structures are directly evaluated by fitting models of the structures to the one-dimensional (1D) SANS/USANS profiles of the dispersed P3HT networks. Scanning TEM (sTEM) and UV−vis spectroscopy (UV−vis) are also utilized to augment and validate the accuracy of the scattering models and to show that solvent choice can have a significant effect on the network structure and affect the resulting electrical properties.

2. EXPERIMENTAL METHODS

2.1. Materials. Sepiolid P200 poly(3-hexylthiophene) (P3HT) was used as purchased from Rieke Metals (Lincoln, NE). The molecular weight (M_w) and polydispersity index (PDI) were characterized using gel permeation chromatography (GPC) and found to be M_w = 24 060 g/mol, PDI = 2.04 with respect to polystyrene standards. The regioregularity of the material was reported by the manufacturer to be greater than 98%. Hydrogenated solvents *p*-xylene, toluene, styrene, and benzene were purchased from Sigma-Aldrich (St. Louis, MO) and used as received. Deuterated solvents D10-*p*-xylene (D > 98%), D8-styrene (D > 98%), D8-toluene (D > 99.5%), and D6-benzene (D > 99.5%) were purchased from Cambridge Isotopes (Andover, MA) and used as received for SANS and USANS experiments to increase the scattering contrast and decrease the incoherent scattering background.

2.2. Sample Preparation. Samples were prepared by adding P3HT to an aromatic solvent and heating to 80 °C until the polymer was fully dissolved (bright orange solution). The polymer solution was then removed from heat, cooled to room temperature, and allowed to crystallize over time. The time required to reach equilibrium varied from 12 h for *p*-xylene samples to 1 week for benzene samples. All samples were made at the same concentration of P3HT (0.2 wt %) unless otherwise stated.

2.3. *Ex Situ* Experiments. Samples were loaded into 100 μm quartz cuvettes and the absorbance was measured using a Thermo Evolution 300 UV−vis spectrophotometer. Images of the crystallites were taken using scanning TEM on a FEI Tecnai G2 F20 instrument and analyzed using Image J software.[18] Samples were further diluted by a factor of 40 prior to deposition onto a TEM grid in order to analyze the structure of the individual colloidal network particles.

2.4. Small-Angle Scattering. Small-angle neutron scattering (SANS) and ultra small-angle neutron scattering (USANS) were performed at the NIST Center for Neutron Research in Gaithersburg, MD. SANS measurements were performed on the NG3 and NG7 instruments using standard configurations to cover a broad q-range ($0.003 < q\ (\text{Å}^{-1}) < 0.3$).[19] SANS experiments were also performed at the ORNL High Flux Isotope Reactor in Oak Ridge, TN. SANS measurements were performed on the CG2 instrument using standard configurations to cover a broad q-range ($0.005 < q < 0.2\ \text{Å}^{-1}$). The 2D scattering profile of the sample, loaded into a 1 mm path length cell, was corrected for background and empty cell scattering and placed on an absolute scale by measuring the empty beam flux.[20] The 2D scattering profile was integrated over the azimuthal angle, and the scattering intensity (I) was plotted against the scattering vector, $q = (4\pi/\lambda)\sin(\theta/2)$, where θ is the scattering angle and λ is the neutron wavelength. USANS measurements were performed at NIST on the BT5 perfect crystal diffractometer further extending the q-range to $4 \times 10^{-5}\ \text{Å}^{-1}$.[21] The data were reduced and desmeared using the NIST Igor-based software.[20] The scattering length density (SLD) of crystalline P3HT was measured to be $0.87 \times 10^{-6}\ \text{Å}^{-2}$ ($\pm 0.1 \times 10^{-6}\ \text{Å}^{-2}$) by contrast variation experiments for colloidal networks in mixtures of hydrogenated and deuterated xylene. This value is somewhat larger than the calculated SLD based on a published crystal lattice and also from neutron measurements on dry solid films ($0.7 \times 10^{-6}\ \text{Å}^{-2}$).[22,23] One possible cause for this could lie in the incorporation of a few solvent molecules into defects in the P3HT fiber structures. Even a very small number of deuterated molecules (1 per 50 P3HT monomer units) would account for this difference in SLD. The experimentally determined SLD was used in all of the calculations. Mathematical model fitting was performed using the NIST Igor-based analysis software as well as the DANSE SansView software.[20]

2.5. Electrical Characterization. The charge transport properties of P3HT networks were characterized by fabricating and testing organic field-effect transistors (OFETs). OFETs were made on a heavily n-doped silicon substrate with a 200 nm thick thermal oxide. The devices were prepared from the same substrate, at the same time and in the same way to ensure that the calculated mobilities would be comparable. Gold source−drain electrodes with a thin chromium adhesive layer were photolithographically patterned on a substrate to define transistor channels with a width of 800 μm and a length of 20 μm. The surface of silicon dioxide was treated with octyltrichlorosilane to promote charge transport. P3HT crystallized in different aromatic solvents was drop-cast onto a substrate in an argon-filled glovebox to minimize insufficient coverage of charge transport channels and to prevent unintentional doping from ambient air. In addition, a P3HT sample in *p*-xylene was heated to 110 °C and spin-coated directly in the amorphous state to serve as a control. Deposited thin films were dried in a vacuum chamber for a few hours. Electrical testing of devices was carried out by using an HP4145B semiconductor parameter analyzer under nitrogen environment. Field-effect mobilities were calculated from the saturation region of the transfer curves.[2,24,25]

3. RESULTS AND DISCUSSION

3.1. P3HT Colloidal Network Morphology. *3.1.1. Fibrillar Structure.* Figure 1 shows the room temperature SANS and USANS profiles for P3HT crystallized from *p*-xylene. The scattering provides structural information over almost 5 orders of magnitude in length scale (about 3 nm to 16 μm) and thus requires different physical models for different size scales.

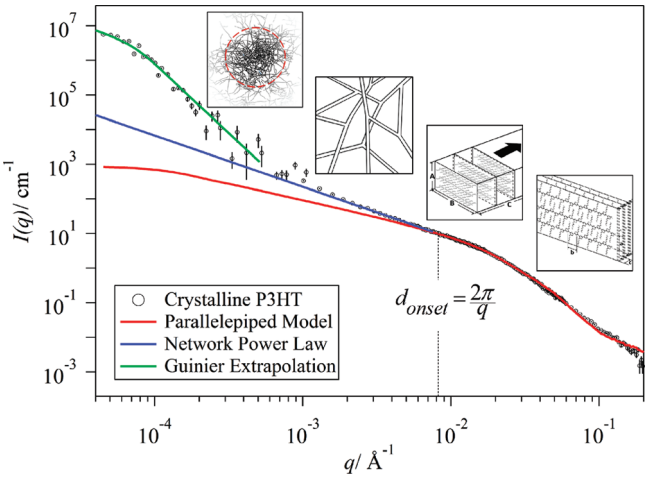

Figure 1. Reduced and combined SANS and USANS data from 0.2 wt % P3HT in *p*-xylene. The data, in absolute scale, are fit using models that describe the structures at different length scales. The insets are schematic representations of the structural features that are characterized at each *q*-range.

The fibrillar cross section of crystalline P3HT in *p*-xylene can be characterized in the range of $0.009 < q\ (\text{Å}^{-1}) < 0.07$ using the parallelepiped model.[26] Chen et al. recently modeled the small-angle X-ray scattering (SAXS) of a P3HT gel with a cylindrical model.[27] However, a parallelepiped model is observed to better represent the orthorhombic crystal structure of P3HT that is reported by many researchers.[10,28,29] The scattering intensity in this region is modeled using

$$I(q) = \phi_v \phi_{PP} (\Delta\rho_{PP})^2 P_{PP}(q) + \phi_v (1 - \phi_{PP})(\Delta\rho_{Amor}) 2 P_{Amor}(q) \quad (1)$$

where ϕ_v is the total volume fraction of P3HT, $\Delta\rho$ is the scattering length density contrast, and ϕ_{PP} is the fraction of the sample that is a parallelepiped shape (i.e., crystalline P3HT). The parallelepiped form factor, $P_{PP}(q)$, is given by

$$P_{PP}(q, A, B, C) = \frac{2}{\pi} \int_0^{2\pi} \int_0^{2\pi} \left[\left(\frac{\sin(qA \sin\alpha \cos\beta)}{qA \sin\alpha \cos\beta} \right) \times \left(\frac{\sin(qB \sin\alpha \sin\beta)}{qB \sin\alpha \sin\beta} \right) \left(\frac{\sin(qC \cos\alpha)}{qC \cos\alpha} \right) \right]^2 \times \sin(\alpha)\, d\alpha\, d\beta \quad (2)$$

where *A*, *B*, and *C* are the fibrillar height, width, and length, respectively. None of the samples are found to completely assemble into nanofibers, leaving some dissolved polymer coexisting with the colloidal networks. At low *q*, the scattering contribution of this soluble fraction is negligible because the fibrillar network dominates the scattering. On the other hand, at very high values of *q*, there is a non-negligible contribution arising from the dissolved polymer fraction. The form factor of the amorphous polymer in solution, P_{Amor}, was measured separately in the fully dissolved samples prior to crystallization. For samples with colloidal networks, the amorphous scattering is scaled by appropriate factors to account for the conservation of total P3HT mass (eq 1), and this contribution is added to the parallelepiped model to account for all scattering objects in solution. This model

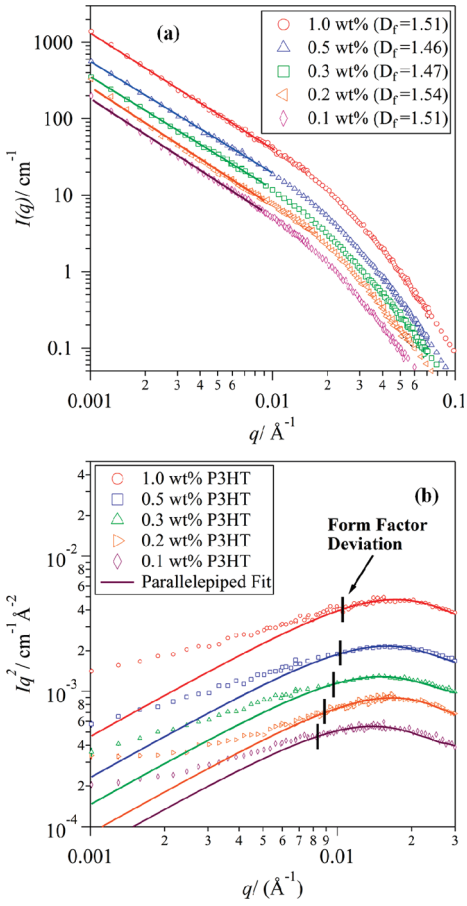

Figure 2. (a) *I* vs *q* scattering profile for P3HT crystallized in *p*-xylene. The power law fit and corresponding fractal dimension are shown for the concentration series. (b) Iq^2 plot of the SANS data, for P3HT crystallized in *p*-xylene, to highlight the "knee" corresponding to the fibrillar cross section and the corresponding parallelepiped model fit. The deviation between the model and scattering is determined from this plot and is utilized to delineate the onset of the fractal region.

is here-in referred to as the parallelepiped fit and the details are further discussed in the Supporting Information (Figure S1).

3.1.2. Network Structure. We also evaluated the fractal nature of the network using a power-law dependence of $I(q) \sim S(q) \sim q^{-D_f}$, where D_f is the fractal dimension.[29] Figure 1 shows a clear deviation between the data and the parallelepiped model fit at $q < 0.0088\ \text{Å}^{-1}$, indicating that, at larger length scales, the scattering is dominated by the network rather than by the form factor of isolated fibers. This region was fit using a power law to obtain a fractal dimension (D_f) that represents the network structure. This physical interpretation is based on the size scale (70−900 nm) over which the self-similar feature exists and is also supported by TEM results that are presented later. The onset of self-similar behavior (d_{onset}) represents the maximum dimension over which the individual fibers in the network can be approximated as isolated rodlike structures.

At the smallest scattering angles in Figure 1 ($q < 4 \times 10^{-4}\ \text{Å}^{-1}$), the data are fit to a Guinier extrapolation because it shows the beginning of a turnover that indicates the maximum size of the colloidal networks. This behavior is attributed to the interface between the colloidal network particles and the solvent. Therefore, this is a surface-dominated scattering region with a

dx.doi.org/10.1021/ma2000515 |*Macromolecules* 2011, 44, 3801–3809

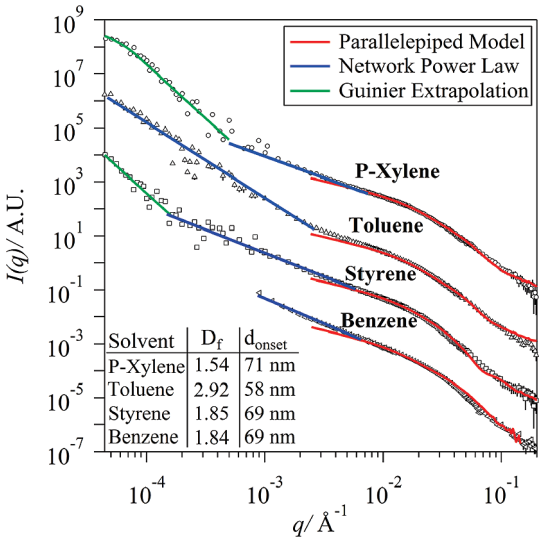

Figure 3. SANS and USANS of 0.2 wt % P3HT crystallized in different aromatic solvents. The parallelepiped fit, power-law fit, and Guinier extrapolations are shown within their appropriate scattering regions. The fractal dimension and the onset of fractal behavior are listed as an inset. USANS data could not be collected for P3HT crystallized in benzene because of the short time frame over which precipitation occurred.

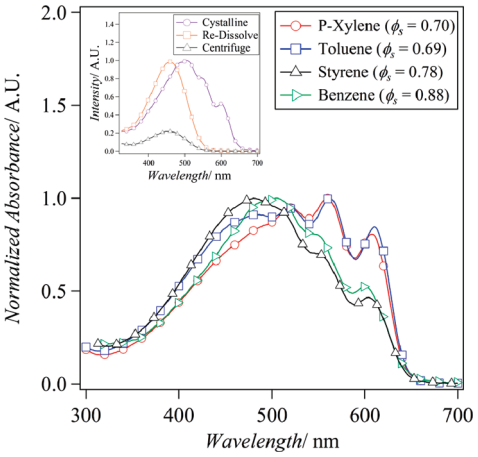

Figure 4. Absorption spectrum of 0.2 wt % P3HT dispersed in different aromatic solvents and allowed to crystallize for 1 month. Inset: absorption spectrum for P3HT crystallized in solution, a crystallized P3HT solution that was redissolved at 80 °C, and the supernatant of a crystallized P3HT solution with solids removed by centrifugation and filtration.

power-law slope that corresponds well with Porod scattering, $I(q) \sim q^{-4}$. The wide range of length scales that are simultaneously analyzed by SANS and USANS in this work (1−10 000 nm) make it essential to use several models to properly analyze the structural features that develop in these complex materials.

Figure 2 shows that the fractal dimension, D_f, is not strongly dependent on concentration over the range of 0.1−1.0 wt %. However, the onset of fractal behavior, d_{onset}, systematically shifts to smaller length scales as concentration increases. This indicates that the fibrillar junctions and the network structure start to affect the scattering data at shorter length scales with increasing P3HT concentration. This corresponds well with the gel-phase concentration dependence that is reported by Koppe and co-workers.[30,31] At 1.0 wt %, P3HT exhibits gel-like elastic behavior at room temperature.

3.1.3. Solvent Dependencies. The structure of crystalline P3HT is strongly dependent on solvent choice, as seen in Figure 3. The fractal dimension (D_f) describes the density of fibers in the network whereas the onset of this fractal behavior (d_{onset}) corresponds to the minimum distance at which fibrillar junctions start to occur. Thus, the combination of D_f and d_{onset} describe the fibrillar junction density over a given length scale. The fibrillar density of an individual network should play an important role in charge transport since it is related to the overall interconnectivity. Samples prepared in toluene have a high fractal dimension ($D_f \sim 3$) and low d_{onset} suggesting the formation of very dense network domains. These network structures are clearly different from those prepared in *p*-xylene where there is a significantly lower fractal dimension ($D_f \sim 1.5$) and high d_{onset}. Unfortunately, the large network features could not be thoroughly evaluated in benzene because USANS data could not be collected fast enough before significant settling would occur.

The persistence of the self-similar behavior toward low q also has important implications for charge transport because it characterizes the overall size of the colloidal network particles. For *p*-xylene and styrene, a surface scattering region ($I(q) \sim q^{-4}$) occurs at the lowest q values and for *p*-xylene a Guinier region is clearly observed in the USANS region. This is ascribed to the scattering from the interface between the colloidal networks and the solvent. In toluene, neither of these features is observed, suggesting that the majority of particles are larger than the measurement range of the USANS configuration.

3.1.4. Total Fiber Fraction and Crystallinity. Fitting the parallelepiped model to the P3HT scattering profiles, with absolute scaling, allows for the determination of the fraction of P3HT that is found in the parallelepiped fibers, ϕ_{PP}. This value can also be obtained independently by removing the solid P3HT network particles from solution, measuring the absorbance of the remaining dissolved P3HT fraction using UV−vis and calculating the concentration of the dissolved phase as seen in Figure 4. The method described by Berson and co-workers for removing solid P3HT from the dispersions, using a combination of centrifugation and filtration, was also utilized here.[32] The samples were also redissolved at 80 °C and the P3HT concentration was measured to corroborate that no evaporative losses occur during the crystallization process. The absorbance values of the original (redissolved) sample and of the supernatant of the separated sample, at the characteristic absorption peak in the amorphous state ($\lambda \sim 450$ nm), were used to calculate the solids fraction (ϕ_s). The results of the two independent analyses are included in Table 1.

$$\phi_s = 1 - \frac{A_{centrifuged}}{A_{redissolved}} \quad (3)$$

The optical transitions associated with P3HT crystallization have been previously characterized in the literature.[11,32] Figure 4 shows the normalized absorbance for P3HT crystallized in solution for all solvents. All of the samples show an optical red shift upon crystallization and confirmation of the presence of interchain $\pi-\pi$ stacking through the characteristic absorbance peak at ~605 nm.[32] However, there is a significant difference in

Table 1. Structural and Charge Transport Properties of P3HT Crystallized in Different Aromatic Solvents

	p-xylene	toluene	styrene	benzene
hole mobility [$cm^2\ V^{-1}\ s^{-1}$]	0.0239 ± 0.0048	0.0305 ± 0.0027	0.0335 ± 0.0049	0.0145 ± 0.0024
threshold voltage [V]	2.0 ± 3.4	0.1 ± 2.5	24.0 ± 6.1	−11.8 ± 6.4
on/off ratio	1.1×10^6	1.4×10^6	2.9×10^4	5.6×10^4
solids fraction (ϕ_{PP},[a] ϕ_s[b])	0.70, 0.70	0.62, 0.69	0.81, 0.78	0.81, 0.88
onset of fractal behavior (d_{onset}) [nm][c]	71	58	69	69
fractal dimension (D_f)[c]	1.54	2.92	1.85	1.84
total fibrillar overlaps per 10 μm fiber length[d]	20	12	11	35
network size [μm][e]	19 ± 7	39 ± 17	35 ± 12	25 ± 11
exciton bandwidth (meV)[b]	60	47	116	112
fiber height [nm][a]	3.8	5.7	8.0	6.5
fiber width [nm][a,d]	17, 28 ± 15	20, 23 ± 8	24, 21 ± 4	24, 30 ± 10

Electrical parameters are averaged from six devices. One standard deviation is also shown for hole mobility and threshold voltage. [a] Obtained from SANS data fitting with parallelepiped model. [b] Obtained from UV−vis spectroscopy. [c] Obtained from SANS and USANS data fitting with power law dependencies. [d] Obtained from sTEM images. [e] Obtained from optical microscopy images.

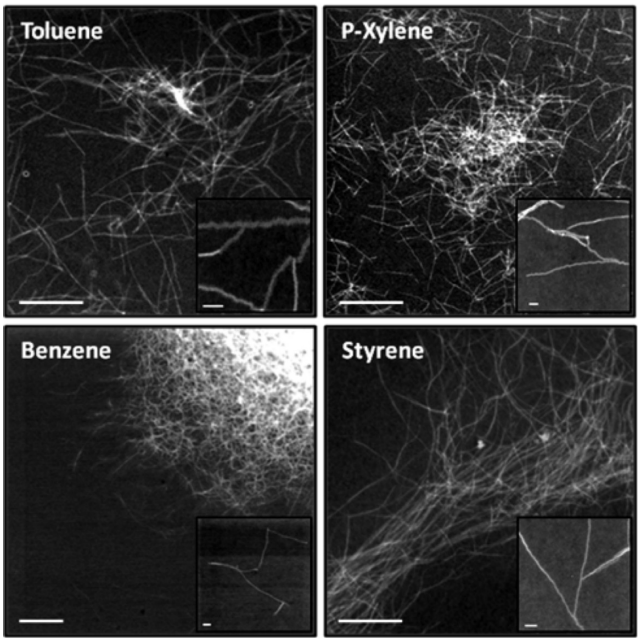

Figure 5. sTEM images of coated colloidal P3HT networks, diluted 40×, crystallized in different aromatic solvents. The primary images highlight the network structure with scale bars at 2 μm. The inset images highlight the fibers with scale bars of 100 nm.

the magnitude of the interchain π-stacking peak depending on the solvent choice.

The crystalline ordering can be quantitatively evaluated using the exciton bandwidth theory developed by Clark and co-workers.[33] The exciton bandwidth (W) was calculated to be 60, 47, 116, and 112 meV for *p*-xylene, toluene, styrene, and benzene, respectively. Lower W values correspond to a more organized structure. P3HT crystallized in *p*-xylene and toluene forms a well-ordered crystalline structure, whereas styrene and benzene samples show significantly lower ordering. The interchain ordering within the crystalline structure can be expected to play a significant role in the charge transport properties of the network.[34] It is important to note that the crystallinity of these samples can only be discussed in the context of the UV−vis spectroscopy and only refers to the interchain $\pi-\pi$ stacking. Fitting the parallelepiped model in SANS provides the fraction of polymer that is in fibrillar form (ϕ_{PP}) but does not provide any quantitative assessment of the P3HT crystallinity within the fibers.

3.1.5. Fibrillar Junction Structure. The structures that were proposed through the analysis of the SANS and USANS data are also in good agreement with the sTEM images of samples that were dilute 40× and coated over grids. The samples were diluted in order to evaluate the structure of the individual network particles. TEM experiments were also performed on the original samples without dilution to verify that the structures did not change during this process (Supporting Information, Figure S2). Figure 5 clearly shows the differences in network densities in the proposed structures. The images also help to illustrate the relationship between the onset of self-similar behavior (d_{onset}) and fibrillar junction density between the networks formed in different solvents. Solvent−polymer interactions lead to a variety of mesoscopic network structures that can be accurately manipulated through small changes in solvent quality. However, these differences could not be correlated exclusively to the solubility of P3HT in the different solvents. On the other hand, the macroscopic phase segregation that exists for benzene samples is most likely related to the limited solubility of P3HT in benzene.

The inset images in Figure 5 highlight the fact that fibrillar bifurcations form regardless of the solvent choice. However, from sTEM, it was clearly more difficult to find this structural feature in styrene samples than in the other samples. This is presumably a result of the higher solubility of the polymer and of its effect on the kinetics of network growth. Figure 6 highlights the three different fibrillar junction types that are present in all samples regardless of the solvent choice. Fibrillar overlap is the most common junction type, and this can be easily distinguished in sTEM. At first inspection, the differences between fibrillar contact and bifurcation can be easily mistaken. However, upon close inspection of the images, it is clear that fibrillar contact is the dominating junction of the two. Bifurcations are desirable because they provide a continuous pathway for charge transport. Recently, Samitsu et al. reported a decrease in hole mobility when comparing P3HT networks to isolated nanofibers.[15] This decrease is attributed to fibrillar overlaps, in good agreement with our finding that colloidal networks of P3HT are dominated by

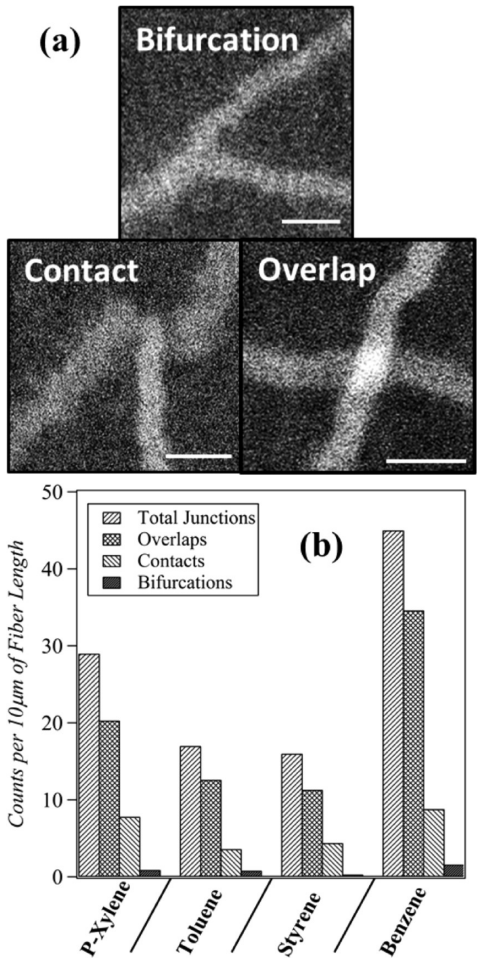

Figure 6. (a) sTEM images of different P3HT fibrillar interactions with scale bars at 50 nm. All samples were crystallized in toluene. (b) The fibrillar length, number of junctions, and type of junction were evaluated from sTEM images. Between 100 and 250 μm of fiber length was measured for each solvent.

fibrillar aggregation rather than bifurcation. Therefore, an ideal network structure would minimize fibrillar overlaps while maximizing bifurcating junctions. It may be possible to further optimize this parameter by controlling the kinetics of network growth.

3.1.6. Network Size. Optical microscopy was also utilized to better determine the size of individual P3HT networks in each solvent, as seen in Figure 7. The samples were diluted 40× prior to deposition and drying on a glass microscopy slide. The drying process did not cause noticeable aggregation due to the small concentration of P3HT after dilution. The network size is found to be strongly dependent on solvent choice with P3HT crystallized in toluene having the largest network size and P3HT crystallized in *p*-xylene having the smallest. The order of colloidal network sizes (*p*-xylene < styrene < toluene) is also well supported by the USANS data even though the resolution was too low to accurately determine the average values for all samples (Figure 3). All four solvents show polydispersity in network size, with toluene being the most significant. The size of an individual network is also expected to play an important role in OFET performance as this parameter determines the minimum number of network particles that are required to create a connection between electrodes. Figure 8b illustrates how larger particles could result in improved performance for OFET devices. Charge transport within a single network particle is expected to be more effective than transport across different particles. Figure 8b is not meant to imply that network particles will form a monolayer structure over the OFET device. This is intentionally drawn in this manner to highlight the finite size of individual network particles. In devices, particles fall on top of each other forming multilayers and they are indistinguishable in TEM.

3.2. Electrical Characterization of Colloidal P3HT. *3.2.1. OFET Performance.* The charge transport of the networks of crystallized P3HT was probed by coating the crystallized network dispersions onto silicon wafers to create organic field effect transistors (OFETs). The OFETs of P3HT crystallized in different solvents showed good current modulation as seen in Figure 8c. The output characteristics of these devices showed linear increase of current at low source-drain bias (V_{ds}) and clear current saturation at high V_{ds} (Supporting Information, Figure S3). The average saturation field-effect mobility of the networks ranged from 1.45×10^{-2} to 3.35×10^{-2} cm^2 V^{-1} s^{-1} with standard deviations of less than 6×10^{-3} cm^2 V^{-1} s^{-1}. The differences in mobility are still evident even when the gate voltages are normalized by the threshold voltages (Supporting Information, Figure S4). In addition to the OFETs made from colloidal networks of P3HT, an OFET was also made by spin-coating the fully dissolved P3HT (amorphous) onto the substrate and allowing the thin film to crystallize after coating. The electrical performance of this amorphous control sample was characterized before and after annealing at a temperature of 150 °C for 10 min. It has been shown that P3HT forms long, overlapping fibers during thin film crystallization and that the overall crystallinity can be increased through annealing after coating.[1,16] The charge carrier mobility and threshold voltage were calculated by using the standard equation for the saturation region, and on/off current ratio was derived from the ratio of maximum current to minimum current.[2,29] All of the relevant electrical and structural parameters are summarized in Table 1.

3.2.1. Implications for the Development of Structure—Property Relationships. The charge-carrier mobility is the parameter that best describes the charge transport through the semiconductor layer. Several of the physical and structural parameters that we have characterized (Table 1) can potentially play important roles in influencing charge transport. Some of these include the total fiber fraction (ϕ_s, ϕ_{PP}), the crystalline order characterized by the exciton bandwidth, the branched structure of the network (D_f, d_{onset}), the type and frequency of interfibrillar junctions (bifurcations, contacts, or overlaps) and the size of the colloidal network particles. Since all of these can affect charge transport, it is very difficult to distinguish the relative importance of each of these features. One of the primary outcomes of this work is to highlight the need for detailed structural characterization spanning over multiple length scales when developing structure—property relationships. Several researchers have reported a strong correlation between P3HT mobility and crystallinity.[1,6] Although we agree that crystallinity is a very important parameter, our results demonstrate that it is difficult to isolate the importance of a single feature without considering structural changes that occur at other length scales. Our observations also show a correlation between exciton bandwidth values (i.e., crystalline order) and hole mobility in network particles that are formed in different solvents. However, the scattering and

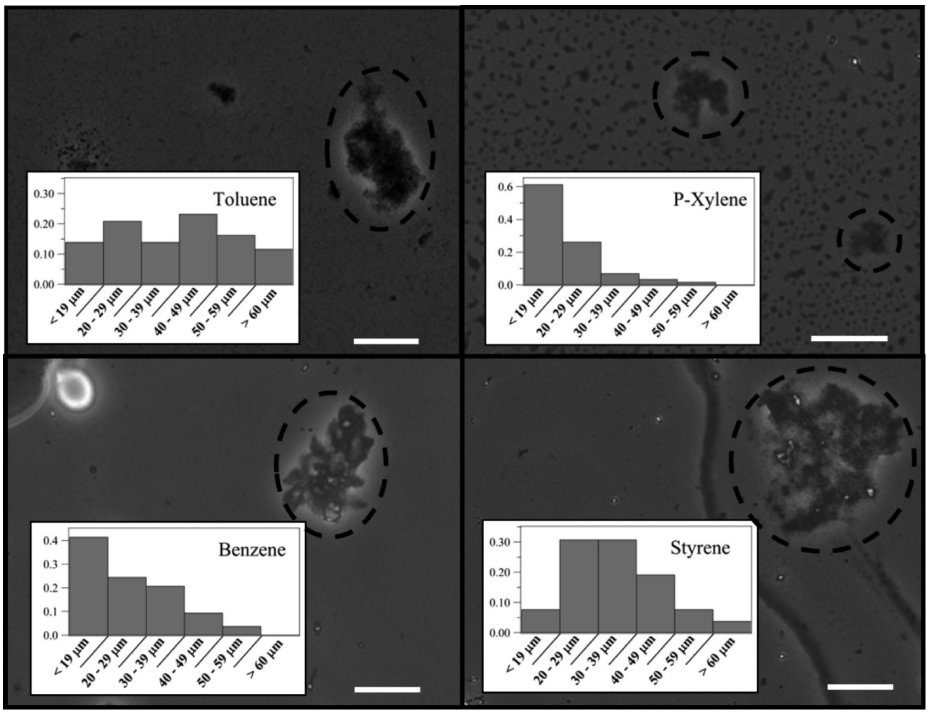

Figure 7. Optical micrographs of coated colloidal P3HT networks taken at 20× magnification, with 10 μm scale bars. Inset: diameter of P3HT networks normalized to the total number of colloidal networks that are counted.

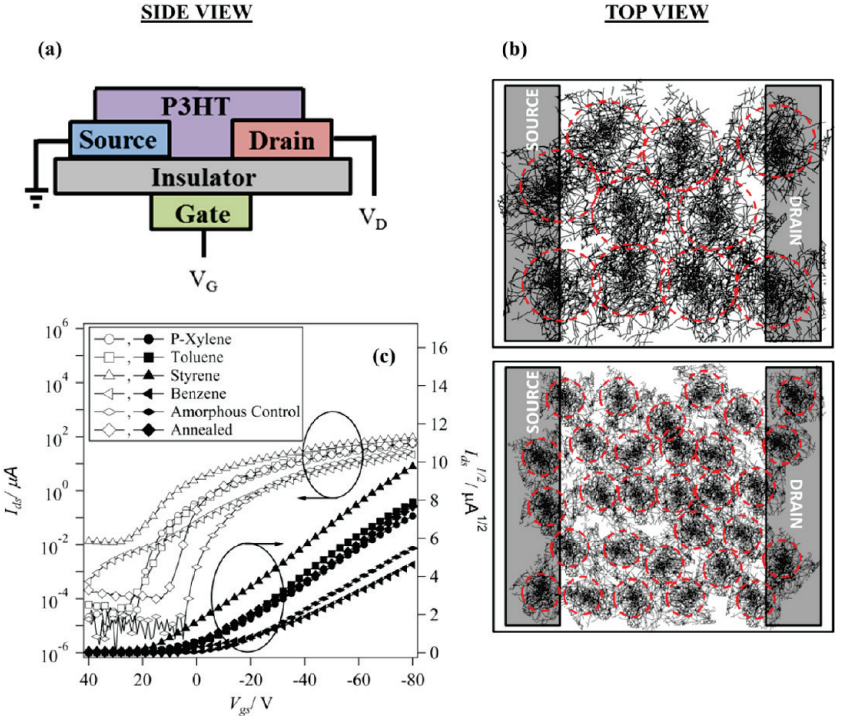

Figure 8. (a) Schematic of an OFET (side view). (b) Effect of network size on the number of colloidal particles required to bridge the electrodes (top view of the OFET). (c) Overlay of OFET transfer curves for P3HT crystallized in different aromatic solvents and control thin films.

microscopy data also demonstrate that the structures are also changing considerably at other length scales.[33] Without the systematic characterization of all relevant length scales, as performed in this study, it would be inappropriate to conclusively identify the crystalline order of P3HT as the primary parameter contributing to improved charge transport.

P3HT networks were previously reported to have a lower mobility than individual nanofibers, and this was attributed to

fibrilar overlaps.[15] Through a detailed analysis of sTEM images, we also find an inverse correlation between the number of fibrillar overlaps and the hole mobility. The size of the colloidal network particles also seems to be correlated with charge transport, given that samples prepared in toluene and styrene have the largest sizes and also the largest mobility values. Presumably, this is due to an effective charge transport mechanism within single network particles and to the smaller number of large colloidal particles that is necessary to bridge the source and drain electrodes in the OFET devices. These combined findings demonstrate that the structure of the networks may also play a significant role in determining charge transport.

It is difficult to draw definitive conclusions from comparison of individual parameters between the networks because of possible interdependencies and competing effects. Still, we expect that the density of fibers in an ideal network, described by D_f and d_{onset}, should be low in order to increase hole mobility. This is due to fibrillar overlaps being the primary junction type and that they could act as effective trap sites. The lowest network density of P3HT particles can be seen in *p*-xylene, followed by styrene and benzene. Networks formed in toluene have a high fractal dimension but sTEM analysis also shows that they have a larger particle size and a lower concentration of fiber overlaps when compared to other particles. The size of the particles should be maximized as this will allow for the network structure to more easily bridge the device electrodes. Although samples in benzene had the highest solid fractions, UV−vis spectroscopy shows that the crystalline order of the solid phase is much lower than *p*-xylene or toluene. The dense junction structure of these samples may also be responsible for the large negative threshold voltage in the OFET measurements by potentially increasing the number of charge transport barriers through imperfect interconnections between fibers. It should also be noted that networks formed in styrene solutions showed off-current values of 10−100 nA, which are 2−3 orders of magnitude larger compared to other samples (0.01−0.1 nA). This large off-current, in conjunction with a large positive threshold voltage of 24.0 V, might come from unintentional doping and can also lead to an overestimation of the intrinsic field-effect mobility.[5]

These results demonstrate the combined importance of crystalline ordering, network structure, particle size, and the dominant type of fiber junctions on charge transport. The hole mobility of solution crystallized samples in toluene and styrene are even higher than those of the thin film crystallized (0.0210 ± 0.0049 cm^2 V^{-1} s^{-1}) and annealed samples (0.0276 ± 0.0057 cm^2 V^{-1} s^{-1}). This suggests that control of crystallinity and network structure of polymer semiconductors crystallized in solution before coating could be an effective means of increasing charge carrier mobility in devices. Furthermore, the formulation of inks based on these colloidal dispersions allows for effective decoupling of the parameters that determine the structure of the networks from those of the coating process. Therefore, the formation of colloidal networks could be an effective and general platform to simplify the fabrication and improve the performance of organic electronic devices.

4. CONCLUSIONS

We have measured and quantified the mesoscale network structure for self-assembled colloidal P3HT and have correlated these to charge transport in OFET devices. The morphology of the P3HT networks were evaluated over multiple length scales through *in situ* SANS and USANS experiments. The relevant structural features were identified to be the crystalline order, the network density, the size of network particles, and the frequency and type of fibrillar junctions. These were all shown to be highly dependent on the choice of solvent that is used to self-assemble the polymer. P3HT fibers were shown to form bifurcating interconnected networks, even though the frequency of actual bifurcations was much lower than the other types of junctions (i.e., contacts and overlaps). OFET measurements were used to compare the structural parameters to performance in real devices. Despite finding clear structure−function correlations, the individual effect of specific parameters cannot be fully established due to nontrivial interdependencies occurring at different length scales. The complexity of the network structures did not allow for the development of simple relationships but did allow us to confirm several design principles. The network density should be low due to the decrease in mobility that results from fibrillar overlaps. However, the size of the individual network particles should be large in order to serve as an effective bridge between the electrode contacts. Intranetwork charge transport is expected to be much faster than internetwork transport. Colloidal P3HT networks represent an important pathway toward simple processing of organic electronic materials. This approach is also demonstrated to be a versatile platform to decouple the parameters that affect polymer self-assembly from those that describe the coating process. These results demonstrate the importance of mesoscale morphology over multiple length scales in developing and optimizing organic electronic devices.

■ ASSOCIATED CONTENT

Supporting Information. P3HT SANS model fitting procedure, OFET output characteristics, and normalized OFET transport characteristics. This material is available free of charge via the Internet at http://pubs.acs.org.

■ AUTHOR INFORMATION

Corresponding Author
*E-mail: dpozzo@u.washington.edu.

■ ACKNOWLEDGMENT

This work was primarily supported by the Department of Energy Office of Basic Energy Sciences under Award DE-SC0005153. G.M.N. also acknowledges support from an IGERT fellowship from NSF DGE Award 0654252, IGERT program on Bioresource Based Energy for Sustainable Societies. We acknowledge the support of the National Institute of Standards and Technology in providing the neutron research facilities used in this work. A portion of this research was conducted at Oak Ridge National Laboratory's High Flux Isotope Reactor that is sponsored by the Scientific User Facilities Division, DOE Office of Basic Energy Sciences. This work benefitted from DANSE software developed under NSF Award DMR-0520547. This work utilized facilities supported in part by the NSF under Agreement DMR-0944772. S.A.J. and F.S.K. acknowledge support from the NSF (DMR-0805259 and DMR-0120967). Part of this work was conducted at the University of Washington NanoTech User Facility, a member of the NSF National Nanotechnology Infrastructure Network (NNIN).

REFERENCES

(1) Yang, X. N.; Loos, J.; Veenstra, S. C.; Verhees, W. J. H.; Wienk, M. M.; Kroon, J. M.; Michels, M. A. J.; Janssen, R. A. J. *Nano Lett.* **2005**, *5*, 579–583.

(2) Bao, Z.; Dodabalapur, A.; Lovinger, A. J. *Appl. Phys. Lett.* **1996**, *69*, 4108–4110.

(3) Yang, X.; Loos, J. *Macromolecules* **2007**, *40*, 1353–1362.

(4) Moule, A. J.; Meerholz, K. *Adv. Funct. Mater.* **2009**, *19*, 3028–3036.

(5) Chang, J. F.; Sun, B. Q.; Breiby, D. W.; Nielsen, M. M.; Solling, T. I.; Giles, M.; McCulloch, I.; Sirringhaus, H. *Chem. Mater.* **2004**, *16*, 4772–4776.

(6) Sirringhaus, H.; Brown, P. J.; Friend, R. H.; Nielsen, M. M.; Bechgaard, K.; Langeveld-Voss, B. M. W.; Spiering, A. J. H.; Janssen, R. A. J.; Meijer, E. W.; Herwig, P.; de Leeuw, D. M. *Nature* **1999**, *401*, 685–688.

(7) Arif, M.; Liu, J. H.; Zhai, L.; Khondaker, S. I. *Appl. Phys. Lett.* **2010**, *96*, 243304–243307.

(8) Merlo, J. A.; Frisbie, C. D. *J. Phys. Chem. B* **2004**, *42*, 19169–19179.

(9) Ihn, K. J.; Moulton, J.; Smith, P. *J. Polym. Sci., Part B* **1993**, *31*, 735–742.

(10) Samitsu, S.; Shimomura, T.; Ito, K. *Thin Solid Films* **2008**, *516*, 2478–2486.

(11) Oosterbaan, W. D.; Bolsee, J. C.; Gadisa, A.; Vrindts, V.; Bertho, S.; D'Haen, J.; Cleij, T. J.; Lutsen, L.; McNeill, C. R.; Thomsen, L.; Manca, J. V.; Vanderzande, D. *Adv. Funct. Mater.* **2010**, *20*, 792–802.

(12) Samitsu, S.; Shimomura, T.; Heike, S.; Hashizume, T.; Ito, K. *Macromolecules* **2008**, *41*, 8000–8010.

(13) Xin, H.; Kim, F. S.; Jenekhe, S. A. *J. Am. Chem. Soc.* **2008**, *130*, 5424–5425.

(14) Xin, H.; Reid, O. G.; Ren, G. Q.; Kim, F. S.; Ginger, D. S.; Jenekhe, S. A. *ACS Nano* **2010**, *4*, 1861–1872.

(15) Samitsu, S.; Shimomura, T.; Heike, S.; Hashizume, T.; Ito, K. *Macromolecules* **2010**, *43*, 7891–7894.

(16) Kim, D. H.; Jang, Y.; Park, Y. D.; Cho, K. *J. Phys. Chem. B* **2006**, *44*, 15763–15768.

(17) Malik, S.; Jana, T.; Nandi, A. K. *Macromolecules* **2001**, *34*, 275–282.

(18) Abramoff, M. D.; Magelhaes, P. J.; Ram, S. J. *Biophoton. Int.* **2004**, *11*, 36–42.

(19) Glinka, C. J.; Barker, J. G.; Hammouda, B.; Krueger, S.; Moyer, J. J.; Orts, W. J. *J. Appl. Crystallogr.* **1998**, *31*, 430–445.

(20) Kline, S. *J. Appl. Crystallogr.* **2006**, *39*, 895–900.

(21) Barker, J. G.; Glinka, C. J.; Moyer, J. J.; Kim, M. H.; Drews, A. R.; Agamalian, M. *J. Appl. Crystallogr.* **2005**, *38*, 1004–1011.

(22) Kayunkid, N.; Uttiya, S.; Brinkmann, M. *Macromolecules* **2010**, *43*, 4961–4967.

(23) Kiel, J. W.; Kirby, B. J.; Majkrzak, C. F.; Maranville, B. B.; Mackay, M. E. *Soft Matter* **2010**, *6*, 641–646.

(24) Kim, F. S.; Guo, X. G.; Watson, M. D.; Jenekhe, S. A. *Adv. Mater.* **2010**, *22*, 478–482.

(25) Guo, X. G.; Kim, F. S.; Jenekhe, S. A.; Watson, M. D. *J. Am. Chem. Soc.* **2009**, *131*, 7206–7207.

(26) Mittelbach, P.; Porod, G. *Acta Phys. Austriaca* **1961**, *14*, 185–211.

(27) Chen, C. Y.; Chan, S. H.; Li, J. Y.; Wu, K. H.; Chen, H. L.; Chen, J. H.; Huang, W. Y.; Chen, S. A. *Macromolecules* **2010**, *43*, 7305–7311.

(28) Liu, J. H.; Arif, M.; Zou, J. H.; Khondaker, S. I.; Zhai, L. *Macromolecules* **2009**, *42*, 9390–9393.

(29) Yang, H.; LeFevre, S. W.; Ryu, C. Y.; Bao, Z. *Appl. Phys. Lett.* **2007**, *90*, 172116–172118.

(30) Koppe, M.; Brabec, C. J.; Heiml, S.; Schausberger, A.; Duffy, W.; Heeney, M.; McCulloch, I. *Macromolecules* **2009**, *42*, 4661–4666.

(31) Malik, S.; Nandi, A. K. *J. Phys. Chem. B* **2004**, *108*, 597–604.

(32) Berson, S.; De Bettignies, R.; Bailly, S.; Guillerez, S. *Adv. Funct. Mater.* **2007**, *17*, 1377–1384.

(33) Clark, J.; Chang, J. F.; Spano, F. C.; Friend, R. H.; Silva, C. *Appl. Phys. Lett.* **2009**, *94*, 163306–163309.

(34) Kim, F. S.; Ren, G.; Jenekhe, S. A. *Chem. Mater.* **2011**, *23*, 682–732.